Distributed Acoustic Sensing along a shallow water energy cable

Nicholas Harmon, Mohammad Belal, Maria-Daphne Mangriotis, Carl Spingys, Catherine A. Rychert

Abstract

Distributed Acoustic Sensing (DAS) provides a means of measuring dynamic changes in strain along a fiber optic cable and has many potential applications for monitoring infrastructure, earthquake early warning, and hazard assessment. Previous work has focused on submarine telecommunications cables, which contain only fiber optic cables. Here we focus on the use of energy cables, which transmit electricity from offshore generators powered by tides or wind but also contain fiber optic cables for communications with the generators. Specifically, we focus on the European Marine Energy Center in Orkney, Eday, UK, a tidal power station. Energy cables fluctuate in temperature due to energy transmission, and there is strong wave action and tidal flows, which all generate noise for DAS. We show noise levels vary along the cable during a time with no energy transmission, but many phenomena reported on telecommunications cables are still observable, including ocean waves and nearby small vessels. The character of the small vessels signals in frequency band energy plots vary along the cable length, in some areas exhibiting multiple frequency band energy peaks. This variation is diagnostic of the burial state of the cable. Burial state of energy cables is important for understanding the mechanical protection of the system for minimizing thermal interactions with the surrounding environments and ecosystems [1].

Manuscript received 11 June 2024, revised 28 October 2024. N. Harmon and C. Rychert are with Woods Hole Oceanographic Institution, Woods Hole, MA, USA and Ocean and Earth Science at the University of Southampton. M. Belal, M. Mangriotis, C. Spingys are with the National Oceanography Centre, Southampton, UK. M. Belal is also with the Department of Mathematical Science at the University of Liverpool and the Department of Physics at the University of Southampton. (email Nicholas.harmon@whoi.edu; mob@noc.ac.uk; Maria-Daphne.Mangriotis@noc.ac.uk; Carl.Spingys@noc.ac.uk; catherine.rychert@whoi.edu;)

I. INTRODUCTION

The advent of the use of submarine fiber optic cables with distributed acoustic sensing (DAS) opens numerous possibilities for understanding the diverse range of biological, anthropogenic, oceanographic and seismic signals that occur beneath the 70% of the planet covered by the oceans. For example, DAS has been demonstrated to be useful for recording and tracking marine mammals in the Atlantic and Pacific Ocean Basins [2-5]. Other studies have demonstrated the ability to track vessels and determine vessel noise characteristics [3, 5-8]. A variety of oceanographic phenomenon have also been studied using submarine DAS, ranging from locally generated and distant storm generated surface gravity waves to tides [5, 8-12]. In addition, microseismic generation and manmade and natural seismic events have been observed using seafloor DAS [5, 8, 10, 13-18].

Much of the previous work has used dark telecoms fiber optic links at 10s of km scale. However undersea power cables, that link offshore infrastructure such as wind or tidal turbines can also carry fiber optic links [19]. Wind and tidal turbines are typically deployed in near shore environments to minimize energy transmission loss and in locations with consistent wind speeds or strong tidal currents [20-22]. These cables provide an excellent opportunity for coastal environmental monitoring of oceanographic phenomenon and acoustic soundscapes. Due to the shallow water, cable design and deployment, and intrinsic thermal fluctuations due to electrical energy transmission, these fiber optic links may be noisier than their telecommunications counterparts. However, it has been demonstrated that DAS using these types of cables can effectively record at least some of the aforementioned signals [6, 9]. In addition, usage on the fiber optic cable is relatively low as they are typically only used for command and control of the offshore infrastructure.

Here we examine the use of DAS on submarine power cables for subsea monitoring, specifically, the European Marine Energy Center (EMEC) in Orkney, Eday (Fig. 1) [23]. We demonstrate that low frequency (< 1 Hz) gravity waves can be observed as well as small vessels. We examine the use of observations of exhibited energy from small vessels in the near field of cable to determine and/or distinguish between the buried and un-buried sections of the cable.

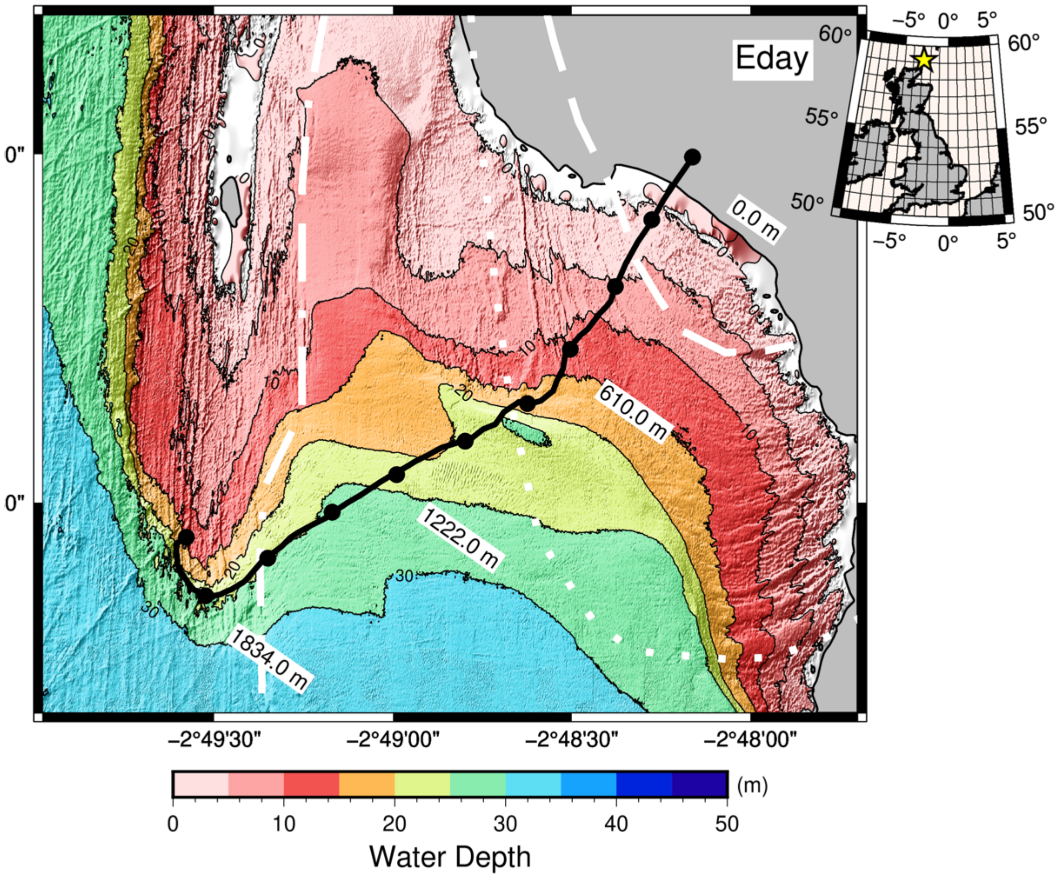

Fig. 1. Map of the study region offshore Eday Island, Orkney, Scotland with cable location. Colored and contoured bathymetric map of the region [24], with the cable shown by the thick black line. Gray colored region indicates land above the mean high tide. Labelled circles indicate the distance along cable used in subsequent figures. Dashed-dotted white line shows geologic boundary between Rousay Flagstones (RF, west) and Lower Eday Sandstone (LE). Dotted white line is the geologic boundary between Lower Eday Sandstone (west) and the

Eday Flagstones (EF). Dashed white line shows the geologic boundary between the Eday Flagstones and the Middle Eday Sandstone (ME). Inset map shows location of EMEC in Scotland, indicated with a yellow star.

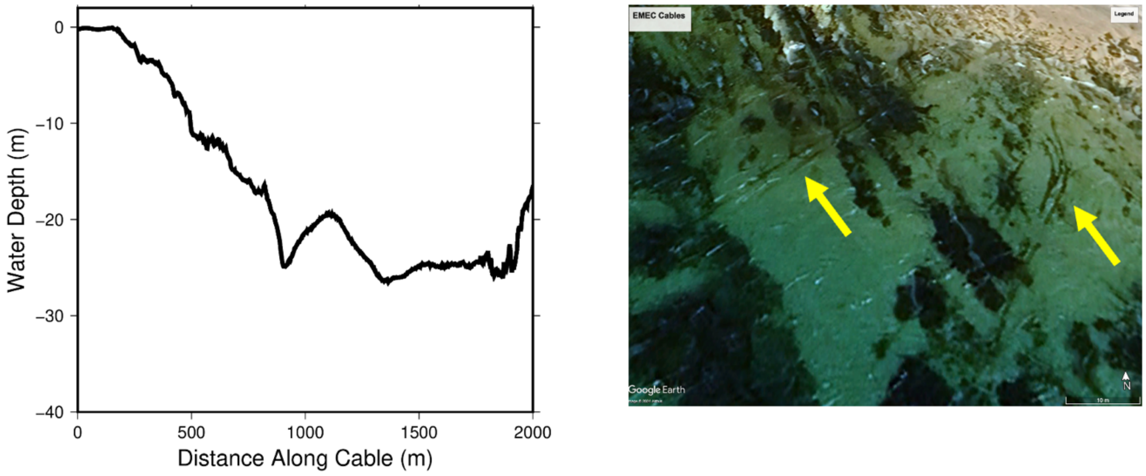

(a) (b)

Fig. 2 Water depth and aerial photography of cable on seafloor (a) Water depth along the cable distance. (b) Aerial photograph of nearshore EMEC site from Google Earth/Airbus [25]. Yellow arrows indicate the locations of cables visible on the seafloor. Cable 4 part of the northernmost cable group.

II. METHODS

A. Site and Cable Description

EMEC provides several test beds for new tidal and wave energy generators, with high voltage cables equipped with fiber optic cables also known as composite cables. The cables comprise three copper high voltage alternative current power lines, and a 12 core single mode fiber optic bundle [19]. The outer diameter of the cable is ~10 cm. The three conductors are near the axis of the cable, whereas the fiber optic cables are located near the outer radius of the cable. The cables are armoured with two layers of steel wire. In shallow water (<15 m) the cables are additionally armoured with ductile iron cable protectors. At the low tide mark the cables are trenched in underground until final termination, but otherwise the cables lie exposed at the seafloor [23]. In this study we use Cable 4 at the Fall of Warness site (Fig. 1) which has a strong tidal current, up to 7.8 knots (~4 m/s) [23]. The cable location was digitized from maps of the cable location at the time it was laid on the seafloor. Therefore, there is some uncertainty in the cable location. Comparison of the digitized cable location relative to the location of the testbed site (where the cable should connect) and EMEC buildings in Google Earth/Airbus aerial photography [25] suggests the error in location is on the order of ± 20 m (Fig. 2b).

The substrate for the cable varies along its length depending on local geology. The cable is located in the Eday Syncline, and variations in seabed geology are visible in the shaded bathymetry due to the variable competence of the rocks [26]. The western most portion of the cable lies within the variable grainsized Rousay Flagstone unit, which is comprised of sandstones dipping to the east (west of the dashed-dotted grey line Fig. 1). The bathymetry beneath this unit is defined by several north-south trending scarps caused by the bedding planes. Immediately adjacent to the east is the fine-grained Lower Eday Sandstone (between the grey dashed - dotted and grey dotted lines Fig. 1, which has been eroded out to form a local embayment and beach. Bathymetric fabric above this unit is smoother in character, partly due to eroded sands covering the unit. Sand ripples are visible in some parts of this unit (north of the 1220.2 m label, Fig. 1) and scour depressions in other parts due to the high tidal velocities. Further east are the Eday Flagstones comprised of some volcanic layers and siltstones/sandstones (between the dashed and dotted lines, Fig. 1 and the medium grainsized Middle Eday Sandstones (east of the dashed line). The bathymetric character of these two units is like the Rousay Flagstones, with scarps due to bedding that curve around to the south, near the nose of the syncline. Visual inspection of aerial imagery over the site (Fig. 2b), shows the cables are exposed on the seabed lying on top of the exposed beds scarps of the

Upper Eday Sandstones and Eday flagstones on the seabed for the ~100 m where the bottom is visible.

B. Acquisition Parameters

The data used in this work were obtained using a DAS system based upon differential Rayleigh phase-based approach (dΦ-DVS) [27], developed as part of the National Oceanography Centre (NOC, UK) intelligent marine fiber sensing research program. The data were acquired using offsite interrogation of the system physically connected to the shore end of ~ 2 km offshore seafloor energy cable. The field campaign was conducted in November 2020. The data were acquired with a gauge length of 10 m, and spatially sampled at 2.04 m along the cable. The sampling frequence was 1000 Hz, with the optical probing routine set to use a single probe frequency. However, there was no energy transmission during the recording period of our experiment.

C. Data Processing, Frequency Band Energy and Spectral Analysis

We present the low frequency DAS signals to highlight oceanographic signals. We detrend and demean the time series. We lowpass filter using an 4th order Butterworth zero phase filter with a cutoff at 0.5 Hz.

We use frequency band energy plots (FBE) to identify small vessels passing near the cable. FBE is a summation across the Power Spectral Density (PSD) of a selected discrete frequency band, with PSD being the power content vs. frequency, which is often used to characterize random processes [28]. FBE analysis has been used in cosmology for applications such as Cosmic Microwave Background (CMB) separation from foreground noise [29] and analysis of cosmological temperature and polarization anisotropies [30], with view to fundamentally isolating the signals from distant astrophysical sources and/or large-scale structure formation. We calculate the FBE plots in the following way. We first detrend the data and then use an 8th order Butterworth zero-phase bandpass filter between 60 – 80 Hz, which encompassed the strongest peak in signal from the small vessel. We then calculate the running median of the envelope of each trace over a 5 s or 2 s window, chosen to enhance presentation at different scales. The envelope is calculated using the absolute value of the complex Hilbert transform pair. The centroid of the energy of the FBE along the fiber provides an approximate location of the small craft at any given time. The rate of change of the centroid along the fiber provides an approximate velocity.

Spectrograms of the traces over different frequency bands are used to explore time variations in the signals of the small vessels. Spectrograms are calculated using short-time Fourier Transforms. A frequency resolution of 0.25 Hz is used with a ~10 s Hann window with 80% overlap. We present estimates of predicted Doppler shifts based on the frequency with the maximum power in the spectrogram. We use the equation:

$$f_O = \frac{c_{water}}{c_{water} + \boldsymbol{r} \cdot \boldsymbol{v_s}} f_S \tag{1}$$

where f_O is the observed frequency at a fixed point on the cable, f_S is the frequency emanating from the source, and c_{water} is the speed of sound in water (1500 m/s), $\mathbf{r}$ is the vector between the source and observed location, and $\boldsymbol{v_s}$ is the velocity vector of the source, or small craft. In addition to the spectrograms, we measure the Doppler shift using the change in instantaneous frequency calculated from the Hilbert transform described above used in the FBE plots.

D. Coupled vs. Uncoupled Fiber Response

The stress and strain on a fiber in response to an impinging plane pressure wave depends on the properties of the medium(s) surrounding the fiber and the incidence angle of the wave. For instance, the cable may be surrounded by the water column or buried or coupled to the Earth. In the water column only normal stresses due to pressure variations can cause strain on the cable as shear is not supported. A buried cable is subjected to both the shear and normal stresses. The stress and strain response of the medium surrounding the cable can be determined from the elastic wave equation and Hooks law.

For a 1-D liquid-solid boundary, the following boundary conditions apply: normal stress is continuous at the boundary, shear stress disappears at the boundary, and normal displacements are continuous at the boundary. We define a two-dimensional coordinate system, $\mathbf{x}_{1,3}$ where direction 1 is horizontal (in line with the fiber) and 3 is vertical. We assume the boundary is at $x_3 = 0$ for convenience. The fluid density (ρ^f) and p-wave velocity (v_p^f) are indicated by a superscript f, while the solid earth half space p-wave velocity (v_p), s-wave velocity (v_s) and density (ρ) are not superscripted. The incidence angle, θ, is relative to the vertical direction (x_3). At a fluid-solid boundary there are three waves generated by the incident P-wave in the water, the reflected P-wave, and the transmitted P and S-waves. We define the following parameters for these waves:

$$p = \frac{\sin\theta}{v_p^f} \tag{2}$$

where p is horizontal slowness of the incident P-wave and is the same for all waves.

$$\eta^f = \frac{\cos\theta}{v_p^f} = \sqrt{\frac{1}{{v_p^f}^2} - p^2}, \tag{3}$$

η^f is the vertical slowness of the incident P-wave.

$$\eta = \sqrt{\frac{1}{v_p^2} - p^2}, \tag{4}$$

η is the vertical slowness of the transmitted P-wave.

$$\eta_S = \sqrt{\frac{1}{v_s^2} - p^2}, \tag{5}$$

η_s is the vertical slowness of the transmitted S-wave.

We also define a denominator for the reflection and transmission coefficients:

$$D = \eta^f\left(-(p^2 - \eta_s)(\rho - 2\rho v_s^2 p^2) + 4\rho v_s^2 p^2 \eta \eta_S\right) + \frac{\rho^f \eta}{v_S^2}. \tag{6}$$

The P-wave reflection coefficient (subscripts denote P incoming and either P or S outgoing) for an incident wave with amplitude A_0 (m^2) is:

$$R_{PP} = \frac{\eta^f\left(-(p^2-\eta_s)(\rho-2\rho v_S^2 p^2)+4\rho v_S^2 p^2 \eta\eta_S\right)-\frac{\rho^f\eta}{v_S^2}}{D} A_0. \tag{7}$$

The transmitted P-wave is given by:

$$T_{PP} = \frac{2\rho^f\eta^f(p^2-\eta_S^2)}{D} A_0. \tag{8}$$

The transmitted S-wave coefficient is given by:

$$T_{PS} = \frac{4p\eta\eta^f}{D} A_0 \tag{9}$$

The displacements in the solid as a function of frequency at $x_3=0$ are given by:

$$u_1(\omega, x_1, p) = i\omega \exp(i\omega(px_1))\,(pT_{PP} + \eta_S T_{PS}) \tag{10}$$

$$u_3(\omega, x_1, p) = i\omega \exp(i\omega(px_1))\,(\eta T_{PP} + pT_{PS}) \tag{11}$$

Strain in the 1 direction in the solid substrate is given by:

$$\varepsilon_{11} = -\omega^2 \mathrm{p} \exp(i\omega p x_1)(pT_{PP} + \eta_S T_{PS}). \tag{12}$$

Pressure in the water at the interface is given by:

$$P(\omega, x_1, p) = \omega^2 \mathrm{\rho}^f \exp(i\omega p x_1)(R_{PP} + A_0). \tag{13}$$

The formulations from Budiansky et al. [31] show a linear relationship between inline strain ε_{11} due to hydrostatic pressure on a two-layer cable is given by:

$$\varepsilon_{11} = \frac{1-2(1-f)\sigma_g - 2f\sigma_p}{fE_g + (1-f)E_p} P \tag{14}$$

where $E_{g,p}$ is the Youngs Modulus of the glass fiber or plastic casing, $\sigma_{g,p}$ is the Poisson's ratio of the glass or plastic coating. The ratio squared of the glass fiber to plastic casing radii is given by f.

The strain on the cable in response to a source with changing incidence angle is expected to be very different if it is in the water (13) or buried (12). If the cable is in the water the energy on the cable should be high at zero incidence angle. Conversely, if the cable is coupled to the seafloor its sensitivity should be zero at zero incidence angle and should increase away from zero incidence. In this paper, we are not focused on the absolute values of strain, but on the relative response between a cable in the water and one just beneath the fluid – solid interface. However, for illustrative purposes, we compare the predicted pressure in the water and the predicted strain in the solid and the strain caused by quasi-hydrostatic loading of the fiber [31] as a function of incidence angles (Fig. 3). We assume the following parameters in the plot: $v_p = 2000$ m/s, $v_s = 1000$ m/s, $\rho = 2000$ kg/m^3, v_p^f=1500 m/s, ρ^f = 2000 kg/m^3, ω=2*π*70 Hz, E_g=64e9 Pa, E_p=.76e9, v_g=.24, and v_p=0.4. We assume $f \ll 1$ in these calculations with a 6 µm fiber and a 2 cm plastic coating.

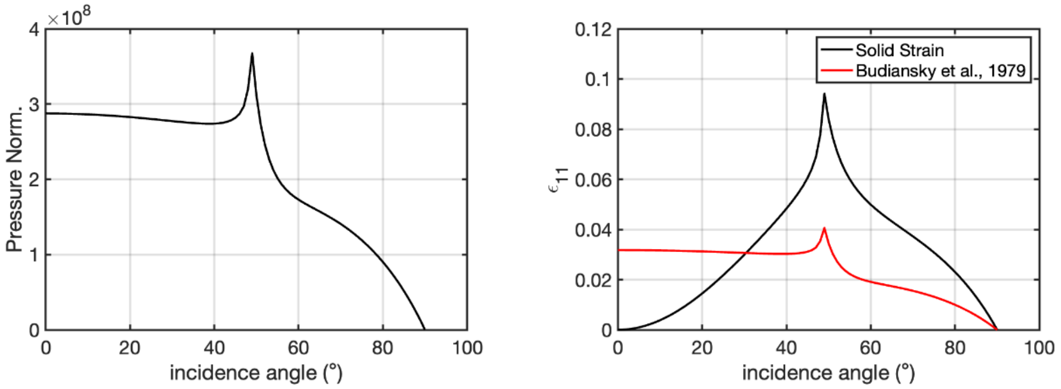

(a) (b)

Fig. 3. Predicted Pressure (a) and predicted inline strain (b). In (b) the red line shows the strain predicted for a cable in the water column using the Budiansky et al. [31] relationship. The black line is the predicted strain in a solid (the Earth) as a function of incidence angle.

III. RESULTS

A. Oceanographic and Small Vessel Signals

Time series at different locations along the cable show clear and coherent signals across a wide frequency range along the length of the cable (Fig 3). At low frequency a .08 Hz (~12 s) signal is visible from approximately 900 – 1800 m distance along the cable with an apparent move out of ~17 m/s, and from 20 – 500 m distance with a slower moveout of ~10 m/s (Fig. 4a). The strength of this signal varies along the distance of the fiber, with 20-500 m and 900-1400 m having particularly high amplitude signals. These signals have a moveout and frequency consistent with shallow water ocean surface gravity waves. In addition, around ~400 s at ~1100 m a coherent wave train with the opposite sense of moveout is visible cutting across the incoming wavefield, which is consistent with reflected ocean gravity waves (Fig. 4a).

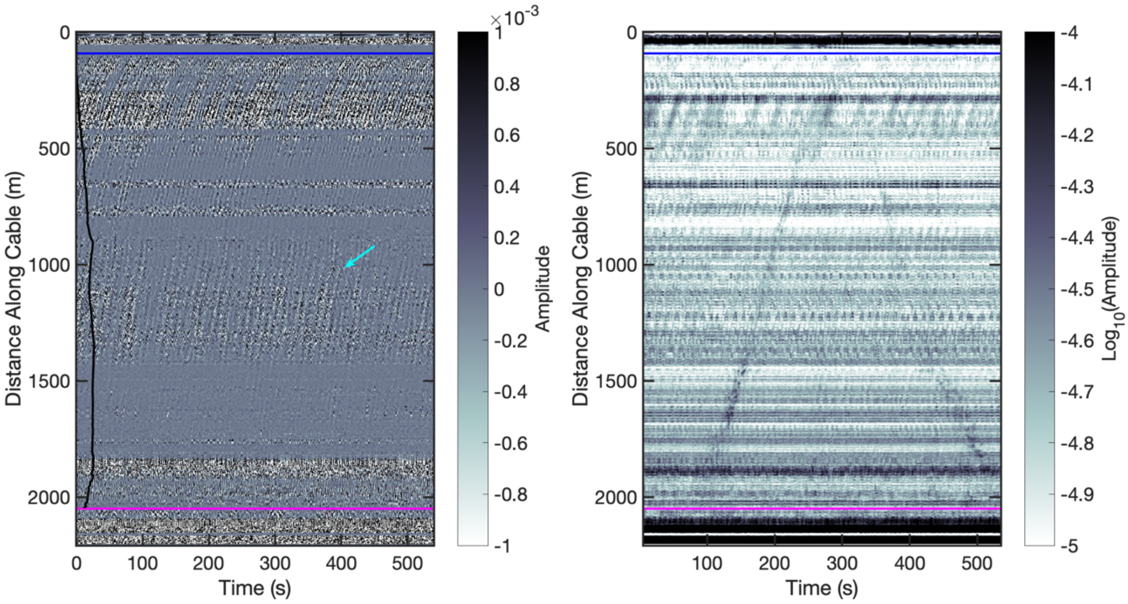

(a)

(b)

Fig. 4. Time series over the length of the cable. (a) Low pass filtered time series data at 0.5 Hz. Cyan arrow indicates location of one refection with opposite moveout (b) FBE plot of energy from 60-80 Hz band pass filtered data showing a small craft passage at ~10 m/s. The

recording time starts on Nov. 12, 2020, 09:16:01.5 GMT. Blue line indicates the land-ocean boundary of the cable, while the magenta line indicates the transition from the ocean to the turbine platform. Thick black line in (a) indicates the water depth in m on the time axis.

In the high frequency FBE plot (Fig. 4b), a narrow (10-30 s) region of high energy (black region) with a moveout of 10-11 m/s is visible between 1800 m and 100 m distance along the cable from 100 to 300 s and with opposite move out from 300 s to 500 s. This signal was generated by a small vessel that steamed along the cable length during the experiment. The vessel was the MV C-Spartan, which is 12 m in length with a 0.8 m draught and a maximum speed of 18 m/s (35 knots). Again, the signal visibility varies along the length of the cable. In contrast to the low frequency signals, the high frequency signals are higher amplitude from 1400 – 1800 m along the cable and muted elsewhere. Both the low and high frequency plots do not have visually coherent signals where the cable changes direction sharply, e.g. ~ 650, 830 and 1834 m. In addition, there is a beating pattern of alternating high and low FBE values, that have a similar moveout to the ~12 s ocean gravity waves.

The average power (modulus of square amplitude) varies along the cable length and shows systematic variations in different frequency bands (Fig. 5). We show examples from two frequency bands of interest, low frequency (<0.5 Hz) to quantify energy changes in ocean gravity wave signals, and high frequency (68-78 Hz) to highlight small craft detectability. We present the average power over a 1-minute window that included ship tracks (Fig. 5 a,b). The power is similar in both plots (10 - 10^3), with both having maxima near 0 m and >2000 m. The maxima are likely the result of increased strain related to the cable hanging from connection points at its endpoints. At low frequencies, power is relatively high (10^3) from 100-500 m distance, where the water depth is < 10 m. It also reaches similar values around ~650 m and ~770 m where the cable changes orientation around a small diversion in the cable. There is also another broad peak from 1000-1300 m (10^3), which is likely related to the favorable slope orientation (dipping towards the incoming waves). The peak is centered on the middle of the shallowing water depth in the 1100-1300 m cable distance range. There are low values (10^1-10^2) from ~1430 – 1817 m, where the bathymetry is relatively flat and smooth and likely sandy. In the un-normalized high frequency power plot, the power is relatively consistent at ~10^3. Power plots normalized by the average power at all frequencies (zero to Nyquist) for each trace are shown for the low frequency (Fig. 5c) and high frequency (Fig. 5d). For the low frequency, very little change is observed in the power along the cable in comparison to the un-normalized case. However, at high frequencies (Fig. 5d), differences between the un-normalized power are visible, particularly from 1450 – 1700 m the power is higher (0.020) than most of the rest of the line (0.002-0.01). In other words, the normalization highlights the region where the ship signal is highest in the FBE plots. In this same region the wave signal power is lower.

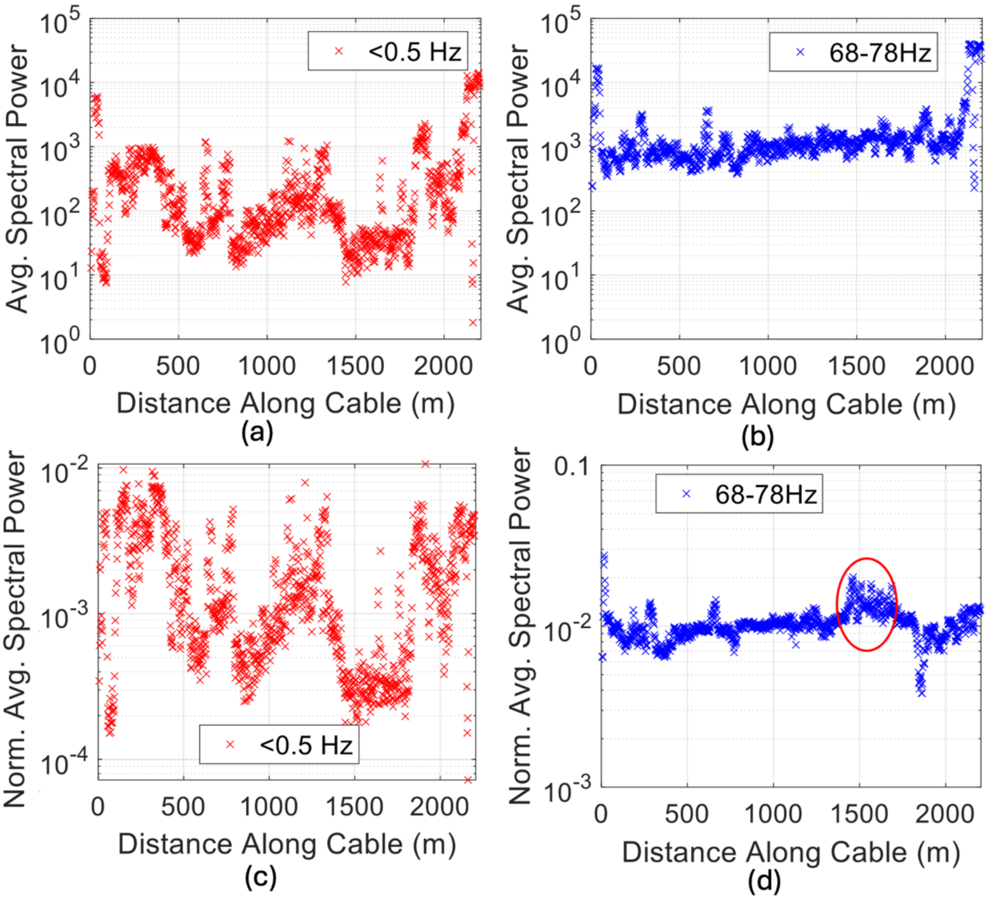

Fig. 5. Averaged power of phase difference in the low-frequency range (up to 0.5Hz) (a) and in the 68-78Hz (b) over a 1-minute phase difference window that included ship tracks. (c) and (d) are the same but normalized using the average of all frequencies. Note that the ship track signature (red circle in d) is only observed in the narrow band 68-78Hz, after normalization by the average power.

The Doppler shift of the small vessel engine signal is visible in spectrograms and in instantaneous frequency plots (Fig. 6). The Doppler shift is particularly pronounced at the speed of the boat (10 m/s, high amplitudes with a similar slope as the white line, Fig. 6 d, 6 e). The small vessel transited along the line of the cable. The shift in frequency ranges from 71.6 Hz to 70.6 Hz with increasing time, which is in good agreement with predictions from

(1) (Fig. 6 a-c) for a path that is aligned parallel to the fiber. The energy in the spectrograms is not a constant as the frequency changes and not necessarily a maximum when the small vessel is closest to the fiber. Rather, some traces have more energy at the extreme values of the doppler shift frequency range, particularly at 1572 m (Fig. 6b). This is likely primarily related to the inline response of fiber optic cables with some contributions from interference effects due to scattering of acoustic energy. The FBE plot shows that there are also several discrete packets of high amplitude for some traces at a given distance along the cable, while other traces only show a single peak in energy, for example at 1389 m (Fig. 6 c, d, e). This change in character in the FBE plots may be related to coupling of the cable, which we explore below. The instantaneous frequency plot (Fig. 6e) shows a relatively wide banded transition between 71.6 Hz to 70.6 Hz (change in color from yellow/orange to green with increasing time), where the FBE energy is high between 1425-1580 m, while outside of this range the difference in frequency range of the Doppler shift is more muted, i.e., a band at 70.25 Hz is visible (green only), typically where only a single packet of energy is visible in the individual traces in the FBE. The range of the Doppler shift we observe 71.6-70.6 would yield a source velocity of ~10 m/s, which is generally consistent with the apparent velocity measured on the FBE (10 m/s line Fig. 6 d,e).

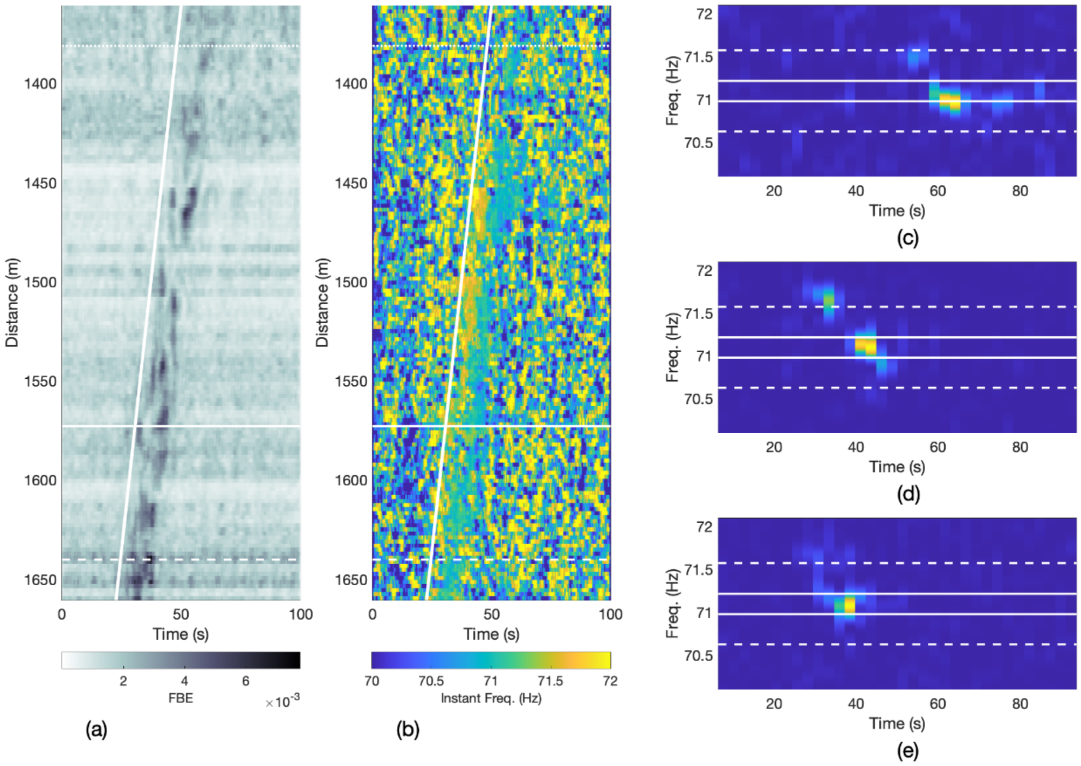

Fig. 6. Doppler shift observations of small craft passing over the cable. Close up view of FBE from 1360 – 1460 m (a). The start time of the plot has been arbitrarily set to 0. Horizontal white lines indicate the location of traces used in (a)-(c), while thick white line indicates at moveout of 10 m/s. Instantaneous frequency of the traces from 1360 – 1460 m (e). White lines same as (d). Spectrograms of individual traces at 1639 m (c), 1572 m (d), and 1389 m (e). White dashed lines indicate predicted Doppler shift for 10 m/s and white solid lines indicate Doppler shift for 2.5 m/s for a center frequency of 71.14 Hz.

B. Modelling of Cable Response to a Small Vessel Source

To illustrate the effects of a moving source on a buried and unburied cable, we generate a simple model for the cable's response to the source in the water column and within the seafloor. The source emits a constant frequency 70 Hz signal, and travels at 10 m/s. The source is located 30 m above the receiver cable and travels inline along the cable (Fig. 7a) for

200 m. To simulate revving of the engine as the vessel pushes through swell we added a 12 s period amplitude modulation to the signal. We assume a point source and calculate the predicted pressure at the seafloor (11), as well as the predicted strain in the solid part of the seafloor (12). We compare the predictions for FBE plots (Fig. 7b, c) to the data (Fig. 7d, e). The FBE plots in Fig. 7 are time shifted by the moving source's speed and summed in the subpanels of Fig. 7 to illustrate the simplified pattern of energy relative to the source's position or incidence angle.

The synthetic examples show distinct patterns in the FBE plots. The buried synthetic FBE generates two maxima, with a minimum energy level in between, centred where the small craft is directly overhead (Fig. 7b). This is because of its sensitivity to ε_{11} in the inline direction of the fiber. When the small vessel is above the fiber it generates little to no ε_{11} strain, whereas at other distances/times there is an increase in amplitude leading up to the critical angle where refraction occurs. The amplitude modulation we apply to simulate engine revving through swell varies the amplitude, producing a diagonal striping in the shifted FBE plots. The summed FBE plot for the buried synthetic shows the two maxima clearly at ~7.5 and 12. 5 s (subpanel Fig. 7b). For the unburied synthetic, there is only a single maximum generated, beneath where the small craft is overhead (Fig. 7c). There is diagonal striping visible in the FBE plots caused by the engine revving amplitude modulation (Fig. 7c). The single peak is visible in the summed FBE (subpanel Fig. 7c). In this case, the pressure signal is greatest at normal incidence and the small vessel's proximity to the cable, causes ε_{11} strain. The lack of coupling results in a scenario where pressure is proportional to the ε_{11} strain.

The observation shows FBE patterns similar to the synthetics for both the buried and unburied case. For example, for the cable between 1500 – 1600 m distance a broad region of energy is visible in the FBE plot from 137 – 152 s (Fig 7d), which when summed results in two peaks at 142 s and 148 s (subpanel Fig.7d). This is like the buried case (Fig. 7b). For the cable between 650-750, the FBE is in a narrower region between 222 – 227 s (Fig. 7e), which when summed produces a single strong peak at 226 s (subpanel Fig. 7e). This is similar to the unburied case's single peak (Fig. 7c)

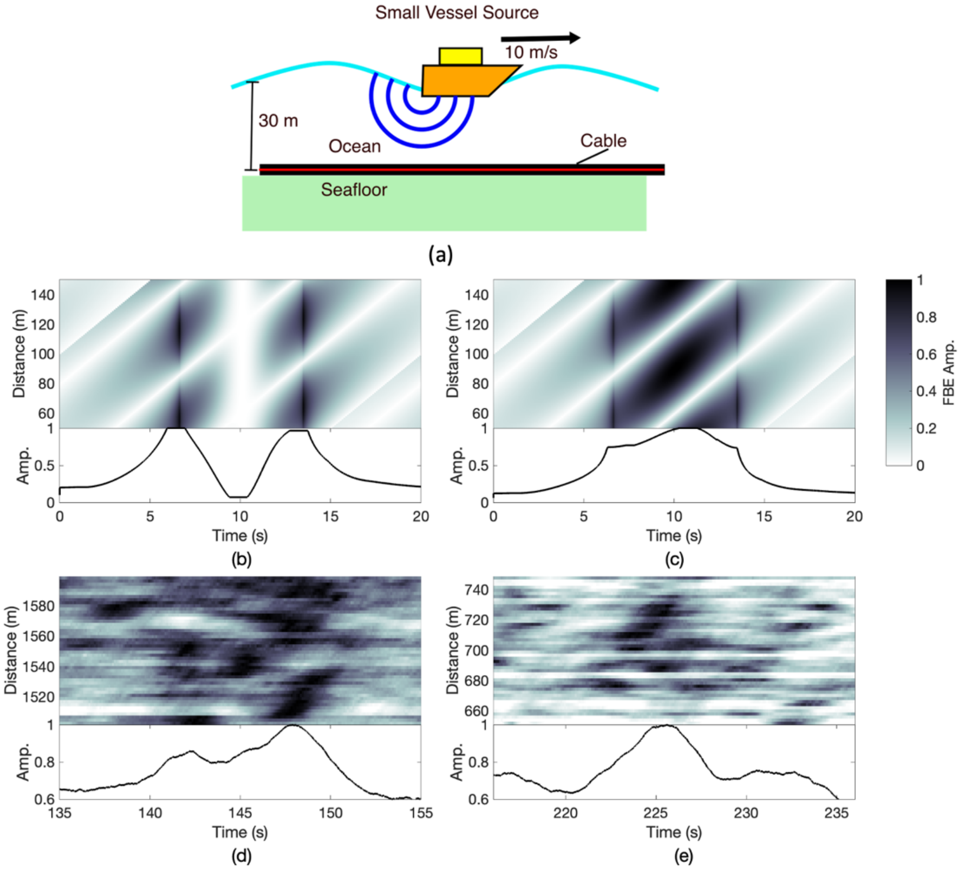

Fig. 7. Synthetic versus observed FBE for suspected buried and unburied fiber on the seafloor. (a) Schematic of moving source model used in the synthetic calculations (a). Synthetic predictions for FBE for a (b) buried and (c) unburied cable on the seafloor. Observed FBE along sections of suspected (d) buried and (c) unburied cable. Top gray-scale subpanels in (b-e) show the moveout corrected FBE. In the observed FBE plots, data are the same as shown in Fig. 4b for the small vessel pass, using the same frequency band of 60-80 Hz. Time is relative to the top trace and the other traces are shifted relative to it. Bottom subpanels in (b-e) show the sum of the move out corrected FBE, to highlight the incidence angle sensitivity of the small vessel signals.

IV. DISCUSSION

Submarine energy cables can observe a broad spectrum of signals. At low frequency (< 0.5 Hz) ocean surface gravity waves are observed across the entire cable. The observed velocity of 9.9-17.2 m/s is consistent with phase velocities for shallow water waves. For shallow water, where the water depth is less than half a wavelength, the surface gravity wave phase speed is given by $c = \sqrt{gh}$ [32] which in this case implied speeds of 17.2 m/s for the offshore locations and 9.9 m/s for the near shore case . The presence of these surface gravity waves also implies oceanographic signals will be present at higher frequencies as these waves undergo non-linear wave breaking and a downscale turbulent energy cascade [33]. This range of processes will result in a higher noise floor from the wave frequency to Kolmogorov scales where viscosity damps the turbulent motions, typically O(1 mm) length scale which, combined with background flow advection of O(1 m/s), implies a frequency of O(1000 Hz) for a fixed position in this environment. At higher frequencies, >10 Hz, the background in the FBE plots exhibits a beating pattern of high and low energy with a period of ~12 s (Fig 3b, 200-500 m), which is likely related to the turbulent energy cascade. In addition, the nearby small vessel is observed. Given the nature of the cable, specifically, that it is designed for energy transfer, laid out on the seafloor over a variably rocky substrate and in a strong tidal-shallow water environment, it is remarkable that these signals are visible.

Our observations of incoming and reflected ocean gravity waves at low frequencies is in line with several previous studies that also observed ocean gravity waves using telecommunications and power cables. For example, shallow water dark communications cables observed ocean gravity waves offshore Belgium and were able to observe both incoming and shore reflected waves using a chirped pulse DAS setup [16]. Our ability to observe the ocean gravity waves opens the potential for investigations of near shore currents using doppler shifts in the wave periods from beamforming, as has been demonstrated offshore Gibraltar on a power cable in 0-150 m water depth [9]. Weak reflections from the shorelines observed here were also observed in other shallow water time series and frequency wave-number plots [9]. Because our cable is in relatively shallow water (<30 m), it is expected that pressure signals from ocean gravity waves should be visible at almost all frequencies where the wavelength is larger than the gauge length. Other studies in greater water depths using bottom pressure records typically detect only low frequency infragravity waves, as expected owing to the frequency dependent decay of a wave's pressure with depth [34-37]. Several other studies have also observed ocean gravity waves locally and from distant storms, determined from long time series and observed dispersion of the wave field over days [5, 8, 10, 11, 15]. Our time series were not long enough to assess the capability of the cable for this type of work.

Our work is also in line with previous work which has observed acoustic sources from vessels and marine life [2-7, 13, 17]. In comparison with previous work the detection range of the small vessel in our region is limited to < 200 m of the cable at a given time, where the signal is spatially coherent and visible by inspection (Fig. 4b and Fig. 6a). Some previous work has shown similar performance to the data presented here, e.g. coherent signal over a few 100s of m [6, 7]. Other work has detected acoustic sources at greater distances, several km or more [2, 3, 13, 17]. Possible explanations for differences in detection distances include the power/strength of the sources, propagation efficiency in the water column, coupling of the cable, cable type or some combination of these factors.

We observe strong variability in the sensitivity of the cable to different sources. Some of the noise due to variability between traces can be attributed to optical polarisation-based fading. The fading occurs due to the use of single optical probe-frequency as probe, which can have destructive interferences in some parts of the cable. Additional contributions to this noise emanate from variability of the substrate and/or coupling of the fiber to the seabed [e.g., 38]. The changes along our cable generally correspond to geological changes along strike of the cable (Fig 1a). Specifically, we observe higher amplitude signals from ocean waves where the cable may be predominantly supported by rock outcrop indicated by scarps in the bathymetry and where slopes face the direction of the incoming wavefield. We observe relatively bright vessel signals on smooth, flat topography.

The cable between 1450 – 1800 m, where the vessel signals have the highest amplitudes, may be partially buried by sediment. There is evidence for sediment transport in the region that may have buried the cable in this location. Inspection of the bathymetry (Fig. 1) reveals the presence of sand waves and scour. This indicates that sediment transport is dynamic in the region due to the high tidal velocities and erosion of the beaches and sedimentary rock formations. Previous studies using submarine cables have also observed sharp changes in the sensitivity [8], and have also suggested variability in the substrate and changing coupling as the likely cause.

In the suspected buried region of the cable the FBE appears to have multiple peaks visible, more apparent when the FBE is corrected for moveout (Fig. 7a top panel) and summed along distance (Fig. 7a bottom panel). In contrast, for a section of cable at the seafloor (650-750 m) the FBE appears to have a single peak (Fig. 7b). This agrees with the predictions in Section II D. Specifically, the cable in the water column can only be strained via pressure variations, specifically normal stress to cable surface, while a buried cable is subject to normal and shear stresses from the surrounding solid medium (Section II D.). Overall, our simple model from section III B captures much of the characteristics observed in the FBE plots from the suspected buried and unburied cable. The agreement between theory and observation here suggests a simple and inexpensive way to test whether a cable is buried or not using local boat traffic. This would obviate the need to dive or send an ROV to inspect the cable.

V. CONCLUSION

We have demonstrated the capability of electrical cables used in offshore energy generation for use in distributed acoustic sensing. These cables were deployed on the seafloor without intentional burial and coupling to the seafloor. The cables are capable of detecting ocean gravity waves propagating towards the coast and reflections. In addition, small craft can be observed and tracked along the cable, and doppler shifts are observed that are related to the velocities of the small craft. The character of the small craft FBE signals change along the length of the cable changing from a single peak in energy to multiple peaks, which can be explained by a change in the burial state of the cable. This later observation provides a means of determining the burial state of the cable.

VI. ACKNOWLEDGMENT

The field work was carried out by NOC as part of project SHARC (Submarine High-fidelity Active-monitoring of Renewable-energy Cables), which was funded by Innovate UK (UKRI file ref: 77739). Some of the data pre-processing and analytics aspects of this work were also supported by UKRI grants (NE/Y003365/1 and NE/Z000408/1). The authors would like to thank the EMEC staff, for their support both in-field and otherwise, during planning and execution of the field campaign at their tidal energy site. We also would like to extend our thanks to Dr. Arthur Hartog and Mr. Alexis Constantinos for discussions on preparation and help during execution of the field campaign.

VII. REFERENCES

[1] J. Lux, M. Olschewski, P. Schäfer, and W. Hill, "Real-Time Determination of Depth of Burial Profiles for Submarine Power Cables," *IEEE Transactions on Power Delivery,* vol. 34, no. 3, pp. 1079-1086, 2019, doi: 10.1109/TPWRD.2018.2881770.

[2] L. Bouffaut *et al.*, "Eavesdropping at the Speed of Light: Distributed Acoustic Sensing of Baleen Whales in the Arctic," (in English), *Frontiers in Marine Science,* Original Research vol. 9, 2022-July-05 2022, doi: 10.3389/fmars.2022.901348.

[3] W. S. D. Wilcock, S. Abadi, and B. P. Lipovsky, "Distributed acoustic sensing recordings of low-frequency whale calls and ship noise offshore Central Oregon," *JASA Express Letters,* vol. 3, no. 2, 2023, doi: 10.1121/10.0017104.

[4] R. A. Rørstadbotnen *et al.*, "Simultaneous tracking of multiple whales using two fiber-optic cables in the Arctic," (in English), *Frontiers in Marine Science,* Original Research vol. 10, 2023-April-28 2023, doi: 10.3389/fmars.2023.1130898.

[5] M. Landrø *et al.*, "Sensing whales, storms, ships and earthquakes using an Arctic fibre optic cable," *Sci Rep-Uk,* vol. 12, no. 1, p. 19226, 2022/11/10 2022, doi: 10.1038/s41598-022-23606-x.

[6] R. Hunt, R. Rogers, and G. Lees, "Listening to your cable with Artificial Intelligence for Assett Monitoring," presented at the 10th International Conference in Insulated Power Cables, Paris, France, 2019.

[7] D. Rivet, B. de Cacqueray, A. Sladen, A. Roques, and G. Calbris, "Preliminary assessment of ship detection and trajectory evaluation using distributed acoustic sensing on an optical fiber telecom cable," *The Journal of the Acoustical Society of America,* vol. 149, no. 4, pp. 2615-2627, 2021, doi: 10.1121/10.0004129.

[8] A. Ugalde *et al.*, "Noise Levels and Signals Observed on Submarine Fibers in the Canary Islands Using DAS," *Seismol Res Lett,* vol. 93, no. 1, pp. 351-363, 2021, doi: 10.1785/0220210049.

[9] E. F. Williams *et al.*, "Surface Gravity Wave Interferometry and Ocean Current Monitoring With Ocean-Bottom DAS," *Journal of Geophysical Research: Oceans,* vol. 127, no. 5, p. e2021JC018375, 2022, doi: https://doi.org/10.1029/2021JC018375.

[10] N. J. Lindsey, T. C. Dawe, and J. B. Ajo-Franklin, "Illuminating seafloor faults and ocean dynamics with dark fiber distributed acoustic sensing," *Science,* vol. 366, no. 6469, pp. 1103-1107, 2019, doi: 10.1126/science.aay5881.

[11] K. Taweesintananon *et al.*, "Distributed acoustic sensing of ocean-bottom seismo-acoustics and distant storms: A case study from Svalbard, Norway," *Geophysics,* vol. 88, no. 3, pp. B135-B150, 2023, doi: 10.1190/geo2022-0435.1.

[12] H. Xiao *et al.*, "Locating the Precise Sources of High-Frequency Microseisms Using Distributed Acoustic Sensing," *Geophysical Research Letters,* vol. 49, no. 17, p. e2022GL099292, 2022, doi: https://doi.org/10.1029/2022GL099292.

[13] H. Matsumoto *et al.*, "Detection of hydroacoustic signals on a fiber-optic submarine cable," *Sci Rep-Uk,* vol. 11, no. 1, p. 2797, 2021/02/02 2021, doi: 10.1038/s41598-021-82093-8.

[14] I. Lior *et al.*, "On the Detection Capabilities of Underwater Distributed Acoustic Sensing," *Journal of Geophysical Research: Solid Earth,* vol. 126, no. 3, p. e2020JB020925, 2021, doi: https://doi.org/10.1029/2020JB020925.

[15] A. Sladen *et al.*, "Distributed sensing of earthquakes and ocean-solid Earth interactions on seafloor telecom cables," *Nature Communications,* vol. 10, no. 1, p. 5777, 2019/12/18 2019, doi: 10.1038/s41467-019-13793-z.

[16] E. F. Williams *et al.*, "Distributed sensing of microseisms and teleseisms with submarine dark fibers," *Nature Communications,* vol. 10, no. 1, p. 5778, 2019/12/18 2019, doi: 10.1038/s41467-019-13262-7.

[17] K. Taweesintananon, M. Landrø, J. K. Brenne, and A. Haukanes, "Distributed acoustic sensing for near-surface imaging using submarine telecommunication cable: A case study in the Trondheimsfjord, Norway," *Geophysics,* vol. 86, no. 5, pp. B303-B320, 2021, doi: 10.1190/geo2020-0834.1.

[18] G. Marra *et al.*, "Ultrastable laser interferometry for earthquake detection with terrestrial and submarine cables," *Science,* vol. 361, no. 6401, pp. 486-490, 2018, doi: doi:10.1126/science.aat4458.

[19] T. Worzyk, *Submarine Power Cables* (Power Systems). Springer Berlin, Heidelberg, 2009.

[20] N. M. Nasab, J. Kilby, and L. Bakhtiaryfard, "Analysis and Design of Monopile Foundations for Offshore Wind and Tidal Turbine Structures," *Water,* vol. 14, no. 21, p. 3555, 2022. [Online]. Available: https://www.mdpi.com/2073-4441/14/21/3555.

[21] T. Asim, S. Z. Islam, A. Hemmati, and M. S. U. Khalid, "A Review of Recent Advancements in Offshore Wind Turbine Technology," *Energies,* vol. 15, no. 2, p. 579, 2022. [Online]. Available: https://www.mdpi.com/1996-1073/15/2/579.

[22] D. Lande-Sudall, T. Stallard, and P. Stansby, "Co-located offshore wind and tidal stream turbines: Assessment of energy yield and loading," *Renewable Energy,* vol. 118, pp. 627-643, 2018/04/01/ 2018, doi: https://doi.org/10.1016/j.renene.2017.10.063.

[23] E. M. E. C. EMEC. "European Marine Energy Centre." https://www.emec.org.uk (accessed 2023).

[24] UKHO. *2005 HI 1122 Sanday Sound to Westray Firth*, 2005. [Online]. Available: https://seabed.admiralty.co.uk/selected-items?x=-304382.19&y=8220780.41&z=11.00

[25] G. E. P. v. 7.3.6.9796. "European Marine Energy Centre, Eday Tidal Energy Test Site, 59° 09’54” N, 2° 48’14” W, elevation 90 m." http://www.google.com/earth/index.html (accessed Nov 10, 2023.

[26] W. Mykura, "Orkney and Shetland. British Regional Geology," ed: HMSO Edinburgh, 1976.

[27] A. H. Hartog, *An Introduction to Distributed Optical Fibre Sensors*, 1st ed. Boca Raton: CRC Press, 2017, p. 472.

[28] S. L. Miller and D. G. Childers, *Probability and random processes : with applications to signal processing and communications*, 2nd ed. Boston, MA: Academic Press (in English), 2012.

[29] P. Collaboration *et al.*, "Planck 2018 results," *A&A,* vol. 641, p. A1, 2020. [Online]. Available: https://doi.org/10.1051/0004-6361/201833880.

[30] C. L. Bennett *et al.*, "NINE-YEAR WILKINSON MICROWAVE ANISOTROPY PROBE (WMAP) OBSERVATIONS: FINAL MAPS AND RESULTS," *The Astrophysical Journal Supplement Series,* vol. 208, no. 2, p. 20, 2013/09/20 2013, doi: 10.1088/0067-0049/208/2/20.

[31] B. Budiansky, D. C. Drucker, G. S. Kino, and J. R. Rice, "Pressure sensitivity of a clad optical fiber," *Appl. Opt.,* vol. 18, no. 24, pp. 4085-4088, 1979/12/15 1979, doi: 10.1364/AO.18.004085.

[32] G. K. Batchelor, *An Introduction to Fluid Dynamics* (Cambridge Mathematical Library). Cambridge: Cambridge University Press, 2000.

[33] C. Spingys, A. Naveira Garabato, and M. Belal, "Distributed fibre optic sensing for high space-time resolution ocean velocity observations: A case study from a macrotidal channel," *Earth Space Science,* 2024, doi: 10.5281/zenodo.7896793.

[34] P. Bogiatzis, A. Karamitrou, J. Ward Neale, N. Harmon, C. A. Rychert, and M. Srokosz, "Source Regions of Infragravity Waves Recorded at the Bottom of the Equatorial Atlantic Ocean, Using OBS of the PI-LAB Experiment," *Journal of Geophysical Research: Oceans,* vol. 125, no. 6, p. e2019JC015430, 2020, doi: https://doi.org/10.1029/2019JC015430.

[35] D. Dolenc, B. Romanowicz, P. McGill, and W. Wilcock "Observations of infragravity waves at the ocean-bottom broadband seismic stations Endeavour (KEBB) and Explorer (KXBB)," *Geochem. Geophys. Geosyst.,* vol. 9, no. Q05007, p. doi:10.1029/2008GC001942, 2008.

[36] N. Harmon, T. Henstock, M. Srokosz, F. Tilmann, A. Rietbrock, and P. Barton, "Infragravity wave source regions determined from ambient noise correlation," *Geophys. Res. Lett.,* vol. 39, pp. L04604, doi:10.1029/2011GL050414, 2012.

[37] J. Neale, N. Harmon, and M. Srokosz, "Source regions and reflection of infragravity waves offshore of the U.S.s Pacific Northwest," *Journal of Geophysical Research: Oceans,* vol. 120, no. 9, pp. 6474-6491, 2015, doi: https://doi.org/10.1002/2015JC010891.

[38] N. J. Lindsey, H. Rademacher, and J. B. Ajo-Franklin, "On the Broadband Instrument Response of Fiber-Optic DAS Arrays," *Journal of Geophysical Research: Solid Earth,* vol. 125, no. 2, p. e2019JB018145, 2020, doi: https://doi.org/10.1029/2019JB018145.